AMERICAN SCIENTIFIC PUBLISHERS

Science of Advanced Materials
Vol. 8, pp. 278–282, 2016
www.aspbs.com/sam

ARTICLE

Ambipolar Properties of Solution-Processed SnO Thin-Film Transistors

Eui-Jung Yun[1,2,*], Jae-Min Song[2], and Byung Seong Bae[3]

[1]*Department of Information and Communication Engineering, Hoseo University, Asan-City, Chungnam 336-795, Korea*
[2]*Department of System Control Engineering, Hoseo University, Asan-City, Chungnam 336-795, Korea*
[3]*Department of Display Engineering, Hoseo University, Asan-City, Chungnam 336-795, Korea*

ABSTRACT

The device properties of solution-processed tin oxide (SnO)-thin-film transistors (TFTs), in which the SnO channel layers were deposited by spin-coating, were investigated. XPS confirmed that the SnO channel layers contained Sn^{2+} and O^{2-} ions in the SnO matrix and were slightly oxygen deficient. The developed SnO-TFTs exhibited good ambipolar properties with almost balanced *p*- and *n*-type parameters, suggesting that in the SnO channel layers, the number of holes arising from tin-vacancies and oxygen-interstitials is identical to that of the electrons resulting from tin-interstitials and oxygen-vacancies. SnO channels with a slight oxygen deficiency might improve the electron field-effect mobility, resulting in balanced field-effect mobilities in the *p*- and *n*-channel operations. The linear dependence of the onset voltage on the drain-to-source voltage was explained using the schematic band diagrams of the SnO-TFTs. The decrease in the on/off ratios with increasing SS was attributed to an increase in the number of trap states at channel/electrodes interfaces caused by an increase in *SS*. This results in a decrease in both the barrier height for hole injection at the source/SnO interface and the barrier height for electron injection at the drain/SnO interface, giving rise to a high off current, which in turn leads to a decrease in the on/off ratios.

KEYWORDS: SnO-Based Oxide TFT, Ambipolar Characteristics, Sol–Gel Process.

1. INTRODUCTION

Recently, solution-processed oxide semiconductors (OSs) by spin coating, dip coating or inkjet printing have been used widely as the channel layer in the fabrication of flexible low-cost thin film transistors (TFTs) because of their chemical stability with respect to oxidation and etching, simplicity, physical robustness, large area coverage, low-cost, and high throughput.[1–4] Ambipolar TFTs, which have both *n*-type and *p*-type active layers in a single TFT with a simplified fabrication process and circuit design, have attracted considerable attention as an alternative approach to realizing radio-frequency identification (RFID) tags or drivers for the next-generation display applications.[5,6] In addition, bipolar OSs, in which both *n*-type and *p*-type carrier doping are allowed in the same material and both types of carriers can be transported freely, are highly desirable for realizing complementary metal-oxide-semiconductor (CMOS)-like devices and circuits,[7–9] which have great advantages over *n*-channel MOS (NMOS), particularly regarding power dissipation and higher density of logic functions on a chip.

To date, only tin monoxide (SnO), $CuInO_2$, ZnO, and LaMnPO are known to be the bipolar OSs.[10] Among them, SnO has attracted considerable attention because it is a good candidate for a *p*-type semiconductors with large hole mobilities owing to its Sn 5*s* nature at the valence band maxima.[8,11–14] This paper emphasize that the spatially spread and spherical Sn 5*s* orbitals, hybridizing and delocalizing O 2*p* orbitals, are isotropic, resulting in a high hole mobility. Moreover, previous studies reported that the wide direct optical band-gap (2.68–2.78 eV) of SnO preserves a rather high transparency in the visible region, whereas the small fundamental band-gap (~0.5 eV) of SnO favors ambipolar behavior.[6]

SnO films have been prepared mainly by several techniques, such as pulsed laser deposition,[10,11] evaporation[12] and radio frequency (rf) sputtering;[13–15] these methods are still far from practical applications. Furthermore, there are few reports on TFTs using a SnO film deposited by a sol–gel process. Therefore, this study examined the device characteristics of TFTs with SnO active layers that were fabricated using a solution-processed method.

*Author to whom correspondence should be addressed.
Email: ejyun@hoseo.edu
Received: 9 December 2014
Accepted: 16 February 2015

2. EXPERIMENTAL DETAILS

The fabrication process of the TFTs is as follows. A sol–gel method was used to prepare the SnO active layers. The precursor solution for the SnO active layer was synthesized by dissolving tin-chloride powder at different concentrations ranging from 0.05 to 0.1 M in 1 M ethanol, which was stabilized with 1 M acetic acid. The precursor solution was stirred for 8 hrs at room temperature (RT), filtered through a 0.2 μm membrane syringe filter and spin-coated at 5000 rpm for 50 sec on the top of a 300-nm-thick SiO_2 dielectric layer grown thermally on a heavily-doped *p*-type Si gate electrode. The SnO prebake process was then performed at 200 °C for 1.5 min. on a hot plate in air to evaporate the solvent. The precursor film was then converted to a 50-nm-thick SnO active layer by annealing at 300 °C for 1 hr in a furnace.

Finally, to fabricate the TFTs, patterned 100 nm aluminum (Al) source and drain electrodes was prepared on the top of SnO active layers through a shadow mask using a thermal evaporator at a pressure of 10^{-6} Torr. The width (W) and length (L) of the samples were 1500 μm and 800 μm, respectively. Figures 1(a) and (b) show a schematic cross-sectional view and a photographic top view, respectively, of typical samples with $W = 1500$ μm and $L = 800$ μm prepared in this study. As shown in Figure 1, the TFTs had a bottom gate and top contact structure. The device characteristics of the SnO-based TFTs were measured at RT in a darkened probe box in air using two Keithley 2400 source meters for the DC voltage source and a Keithley 6485 picoammeter for the current measurements along with the corresponding software (Microsoft visual basic). The capacitances of the SiO_2 gate dielectric films were measured at RT using an Agilent 42854A precision LCR meter after forming Ohmic contact with a 150-nm-thick Mo layer deposited by DC magnetron sputtering. X-ray photoelectron spectroscopy (XPS) was conducted to examine the contents (at.%) and the Sn and O chemical bonding states in the SnO films.

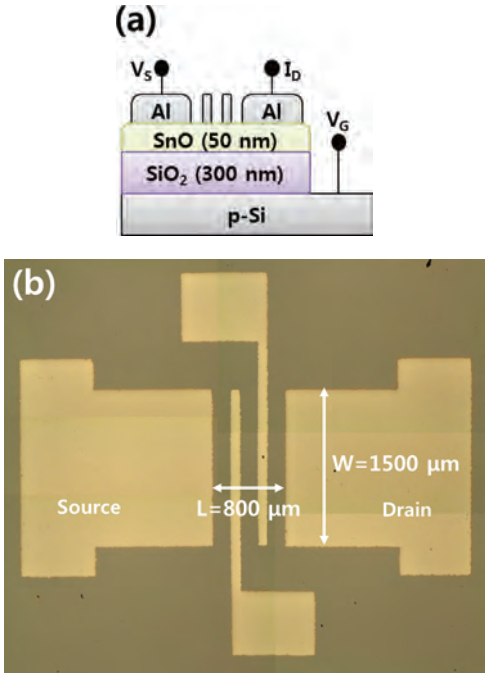

Fig. 1. (a) Schematic cross-sectional view and (b) photographic top view of the solution-processed SnO-TFTs developed in this study: $W = 1500$ μm and $L = 800$ μm.

3. RESULTS AND DISCUSSION

The raw XPS data indicated that considerable electrostatic charging took place because of the nonconducting substrates used. Therefore, the observed spectra was calibrated using the C_{1s} peak (284.6 eV) as the reference. To obtain the correct chemical composition of the bulk layer of the SnO films, high doses of argon ions were also used to sputter away the top layer (~4 nm). Figure 2 shows the calibrated XPS results for the Sn 3*d* core level obtained from the solution-processed SnO thin-films prepared with a tin-chloride concentration of 0.1 M and an annealing temperature of 300 °C. The etched SnO film surface showed a spin-orbit doublet at ~485.6 and ~494.1 eV, which were assigned to Sn^{2+} $3d_{5/2}$ and Sn^{2+} $3d_{3/2}$, respectively.[6, 16, 17] This suggests that the Sn 3*d* core level XP spectra of the etched sample only present one peak corresponding to Sn in the SnO matrix.

Figure 3 also shows the results of XPS analyses for the O 1*s* core level obtained from the solution-processed SnO thin-films prepared with a tin-chloride concentration of 0.1 M and annealing temperature of 300 °C. The O 1*s* peak was fitted by two Gaussian peaks (GPs). For all SnO films, one dominant GP at approximately 529.5 eV (peak 1), which was attributed to O in SnO,[6, 16, 17] was observed and an additional GP was centered at around 530.9 eV (peak 2), which was assigned to adsorbed O on

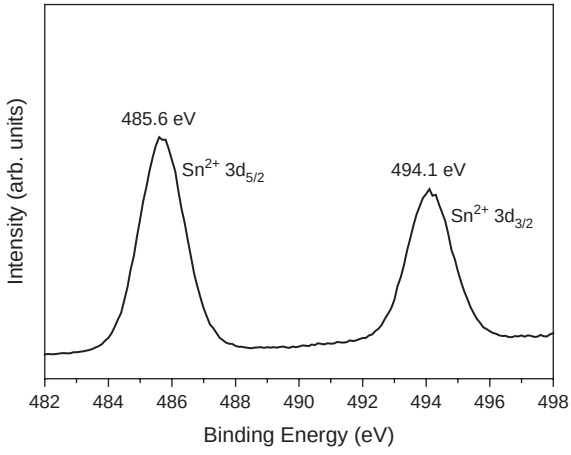

Fig. 2. Sn 3*d* core level narrow scan XP spectra of the solution-processed SnO thin-films prepared with a tin-chloride concentration of 0.1 M and annealing temperature of 300 °C.

ARTICLE

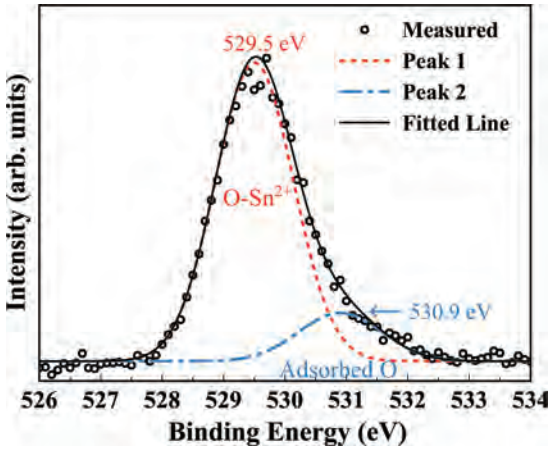

Fig. 3. O 1*s* core level narrow scan XP spectra of the solution-processed SnO thin-films prepared with a tin-chloride concentration of 0.1 M and an annealing temperature of 300 °C.

the outermost surface near the film surface. This indicates that the oxidation of SnO films occurs near the surface of the films. The content (at.%) of the samples obtained from XPS indicated that the Sn/O atomic ratio of the calibrated sample was determined to be 52.95/47.05, suggesting that the SnO channel layers were slightly oxygen deficient.

Figure 4 shows the typical source-to-drain current versus gate-to-source voltage (I_{SD}–V_{GS}) transfer curves of the TFTs fabricated with the solution-processed SnO channel layers, which exhibited the XPS characteristics shown in Figures 2 and 3. Here, a series of measurements were performed with different drain-to-source (V_{DS}) voltages ranging from −0.01 to −10 V, which are in the sub-threshold and saturation regions. The sub-threshold swing in *p*-type operation (SS_p), which describes the change in V_{GS} that should be applied to the devices to increase I_{SD}

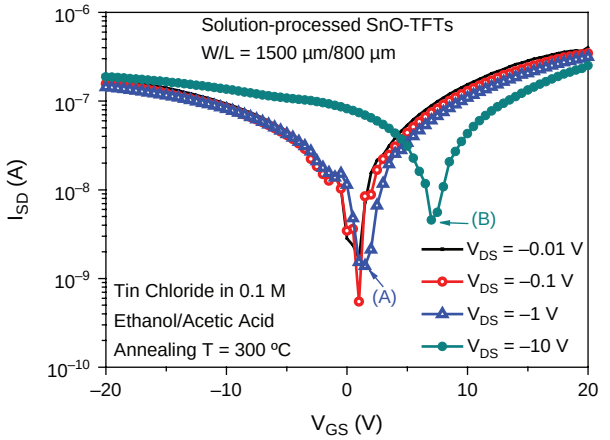

Fig. 4. Typical I_{SD}–V_{GS} transfer curves of the TFTs fabricated using solution-processed SnO channel layers, which have XPS characteristics shown in Figures 2 and 3. The V_{DS} values were varied from −0.01 to −10 V. The point (A) has a low V_{ON} value of ~0 V and is in the linear region with a low $|V_{DS}|$, whereas the point (B) has a high V_{ON} value and is in the saturation region with a high $|V_{DS}|$.

by an order of magnitude, of the same devices used in Figure 4 was also obtained from the inverse slope of the curve shown in Figure 4 using Eq. (1)[18, 19]

$$SS_p = \left[\frac{d(\log I_{SD})}{dV_{GS}}\right]^{-1} \quad (1)$$

The sub-threshold swing in *n*-type operation (SS_n) can also be obtained if I_{SD} is replaced with I_{DS} in Eq. (1). If the device operates in sub-threshold mode, the linear-region hole field-effect mobility, $\mu_{\text{l-hole}}$, in *p*-type operation can be estimated using Eq. (2)[20]

$$\mu_{\text{l-hole}} = \frac{\partial I_{SD}}{\partial V_{GS}} \frac{L}{W} \frac{1}{C_{SiO_2}} \frac{1}{V_{SD}} \quad (2)$$

where C_{SiO_2} is the capacitance per area of the SiO_2 gate insulator, which was 11.5 nF/cm^2, as measured in a metal-insulator-metal configuration. The linear electron field-effect mobility, $\mu_{\text{l-electron}}$, in *n*-type operation can also be estimated using Eq. (2) if I_{SD} and V_{SD} are replaced with I_{DS} and V_{DS}, respectively. The saturation hole field-effect mobility, $\mu_{\text{s-hole}}$, was calculated using

$$\mu_{\text{s-hole}} = \left(\frac{\partial\sqrt{I_{SD}}}{\partial V_{GS}}\right)^2 \frac{2L}{W} \frac{1}{C_{SiO_2}} \quad (3)$$

The saturation electron field-effect mobility, $\mu_{\text{s-electron}}$, in *n*-type operation can also be estimated using Eq. (3) if the I_{SD} and V_{SD} are replaced with I_{DS} and V_{DS}, respectively.

Table I lists important device parameters of the solution-deposited SnO-based TFTs as a function of V_{DS}, which were obtained from the results in Figure 4 using Eqs. (1)–(3). As shown in Figure 4 and Table I, the solution-processed SnO-based TFTs exhibited ambipolar properties, which have near balanced *p*- and *n*-type parameters. The onset voltage (V_{ON}), which is defined as $|V_{GS}|$ at which the mobile hole or electron carriers begin to accumulate in the channel and $|I_{DS}|$ begins to increase in a transfer curve, was also found to be close to zero at very low V_{DS} values of −0.01 and −0.1 V. This reflects the symmetry of the ambipolar TFT and supports the ambipolar operation of the developed SnO-TFTs. Here, V_{ON} was used rather than the threshold voltage because V_{ON} is determined mainly by the trapped charges, whereas shifts in the threshold voltage in TFTs can be related to changes in many more physical parameters, such as *SS* and the mobility.[21, 22] In the SnO channel layers of the developed TFTs the number of *p*-type carriers originating from tin vacancies (V_{Sn}) and oxygen interstitials (O_i) are almost identical to those of the *n*-type carriers resulting from tin interstitials (Sn_i) and oxygen vacancies (V_O).[23] As listed in Table I, ambipolar conduction with well-balanced *p*- and *n*-type field-effect mobilities was observed in the developed SnO-TFTs. The SnO channels with a slight oxygen deficiency, as evident in these XPS results, might benefit the improvement of the electron field-effect mobility, resulting in balanced field-effect mobilities in the *p*- and *n*-channel operations in this work.

Table I. Summary of the important device parameters of the developed SnO-TFTs as a function of V_{DS}, which were obtained from the results in Figure 4 using Eqs. (1)–(3).

V_{DS} value applied to the SnO-TFTs (V)	V_{on} (V)	*p*-type parameter			*n*-type parameter		
		μ_{hole} (cm^2/Vs)	$I_{on/off(p)}$	SS_p (V/dec.)	$\mu_{electron}$ (cm^2/Vs)	$I_{on/off(n)}$	SS_n (V/dec.)
−0.01	1	43.8[(a)]	108	3.14	50.3[(c)]	242	1.24
−0.1	1	4.1[(a)]	285	1.26	6.7[(c)]	630	0.42
−1	1.5	0.44[(a)]	104	1.77	0.59[(c)]	227	1.69
−10	7	0.62[(b)]	41.1	3.55	0.32[(d)]	55.2	3.24

Notes: (a) Indicates the linear-region hole field-effect mobility. (b) Indicates the saturation-region hole field-effect mobility. (c) Indicates the linear-region electron field-effect mobility. (d) Indicates the saturation-region electron field-effect mobility.

Another ambipolar operation was observed[17] in the reactive sputter-deposited SnO-TFTs using a Sn target at 90 °C and an oxygen partial pressure of 6.0% after annealing at 260 and 290 °C in air ambient. A previous study reported[23] that the ambipolar behavior in SnO-TFTs can be attributed to the bipolar nature of the SnO channel.

Figure 4 and Table I also show that the V_{ON} values change significantly, depending on the V_{DS} value and the linear dependence of V_{ON} on V_{DS} at a negative V_{DS} is depicted in Figure 5. In Figure 5, the open circle symbol indicates the measured V_{ON} values for the samples and the solid line shows the best linear fit to the measured V_{ON} values for the samples. As shown in Figure 5, the V_{ON} value shifted to the positive position as the magnitude of the negative applied V_{DS} increased, indicating that V_{ON} depends linearly on $|V_{DS}|$.

To realize good ambipolar TFTs, the efficient and balanced injection of both electrons and holes from the source/drain (S/D) electrodes into a channel layer or vice versa is necessary.[6] Therefore, a channel with small band-gap and suitable band alignment matching between the S/D electrodes and semiconductor channel contact should be selected to reduce the injection barrier. The SnO channel is likely to be the best choice because it has a low fundamental band-gap of 0.5 eV.[6] This SnO also reduces the technical difficulties in selecting the S/D electrode materials. In this study, the commonly used Al S/D electrodes, which have a work function of 4.26 eV, were utilized.[24] Figure 6 shows a schematic band diagram of the SnO-TFTs at different V_{ON} corresponding to two points, (A) and (B), as highlighted in Figures 4 and 5. At point (A), which has a low V_{ON} value of ~0 V and is in the linear region with low $|V_{DS}|$, the band bends slightly at both the source/SnO and drain/SnO interfaces, balanced charge injection occurs due to the formation of the same injection barriers at the electrode/SnO interfaces. With the applied low $|V_{DS}|$, the Fermi level (E_F) of the S electrode decreases slightly compared to that of SnO, which lies in the middle of the band-gap of SnO, whereas the E_F of the D electrode increases slightly compared to that of SnO. This results

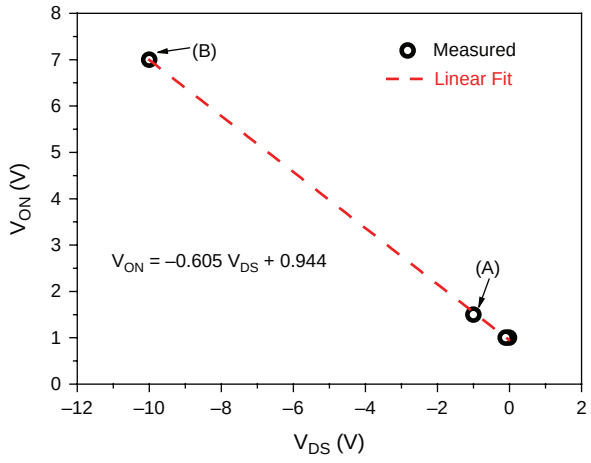

Fig. 5. Linear dependence of V_{ON} on V_{DS} at negative V_{DS} for SnO-TFTs prepared in this work: the open circle symbol indicates the measured V_{ON} values for the samples and the solid line shows a best linear fit to the measured V_{ON} values for the samples. The point (A) has a low V_{ON} value of ~0 V and is in the linear region with a low $|V_{DS}|$, while point (B) has a high V_{ON} value and is in the saturation region with a high $|V_{DS}|$.

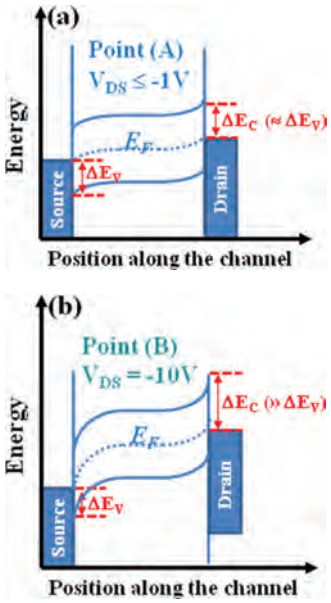

Fig. 6. Schematic band diagram of the SnO-TFTs at different V_{ON} corresponding to two points, (A) and (B), highlighted in Figures 4 and 5. The point (A) has a low V_{ON} value of ~0 V and is in the linear region with a low $|V_{DS}|$ while the point (B) has a high V_{ON} value and is in the saturation region with a high $|V_{DS}|$.

ARTICLE

in an identical barrier height for hole injection at the source/SnO interface (ΔE_V) to that for electron injection at the drain/SnO interface (ΔE_C). As a result, the positive V_{GS} to turn on the SnO-TFTs for the *n*-channel operation would be the same as the negative V_{GS} for *p*-channel operation, which in turn leads to a low V_{ON} value of ~0 V (See Fig. 6(a)). On the other hand, at point (B), which has a high positive V_{ON} value and is in the saturation region with a high $|V_{DS}|$, the band at the source/SnO interface bends more severely than that at the drain/SnO interface, higher hole injection than the electron injection occurs due to the formation of a lower ΔE_V at the source/SnO interface. With the application of a high $|V_{DS}|$, the E_F of the S electrode decreases significantly compared to that of the SnO, whereas the E_F of the *D* electrode increases moderately. This results in a much smaller ΔE_V than ΔE_C, correspondingly, the V_{ON} value would be highly positive when a high $|V_{DS}|$is applied, which agrees with these observations.

As listed in Table I, the on/off ratios in the *p*- and *n*-type operations ($I_{on/off(p)}$ and $I_{on/off(n)}$) decreased with increasing SS in both *p*- and *n*-type operations. An increase in the *SS* is related to an increase in the density of subgap trap states at the E_F, which are located close to the semiconductor/insulator or semiconductor/electrodes interfaces.[25] The presence of subgap trap states at the SnO/electrode interfaces will reduce both ΔE_V and ΔE_C, resulting in a high off current, which in turn leads to a decrease in the on/off ratios.

4. CONCLUSION

This study examined the device characteristics of TFTs with SnO channel layers fabricated using a solution-processed method. XPS of the SnO channel layers revealed Sn and O atoms in the SnO matrix and a slight oxygen deficiency. The developed SnO-TFTs exhibited ambipolar properties, which have near balanced *p*- and *n*-type parameters. The results suggest that in SnO channel layers of the developed TFTs, the number of holes originating from V_{Sn} and O_i is similar to that of the electrons resulting from Sn_i and V_O. In addition, SnO channels with slight oxygen deficiency, as shown by XPS, might benefit from an improvement in electron field-effect mobility, resulting in balanced field-effect mobilities in *p*- and *n*-channel operations. Schematic band diagrams of the SnO-TFTs were derived to explain the linear dependence of V_{ON} on $|V_{DS}|$: In the case of a low V_{ON} and a low $|V_{DS}|$, the ΔE_V is similar to the ΔE_C, resulting in a positive V_{GS} to turn on the SnO-TFTs for *n*-type operation that would be close to the negative V_{GS} for the *p*-type operation, which in turn leads to a low V_{ON}. On the other hand, for a high positive V_{ON} and a high $|V_{DS}|$, ΔE_V is much smaller than ΔE_C. This results in a positive V_{GS} for *n*-type operation that would be much greater than the negative V_{GS} for *p*-type operation. Consequently, the V_{ON} value would be highly positive. The decrease in on/off ratios with increasing *SS* is likely to be because an increase in the number of trap states at the semiconductor/electrodes interface caused by an increase in the *SS* results in a decrease in both ΔE_V and ΔE_C, giving rise to a high off current, which in turn leads to a decrease in the on/off ratios.

Acknowledgments: This study was supported by the Academic Research Fund of Hoseo University in 2014 (FRC-2014-0082).

References and Notes

1. Y. B. Yoo, J. H. Park, S. J. Lee, K. M. Song, and H. K. Baik, *Jpn. J. Appl. Phys.* 51, 040201 (**2012**).
2. Y. H. Hwang, S.-J. Seo, J.-H. Jeon, and B.-S. Bae, *Electrochem. Solid-State Lett.* 15, H91 (**2012**).
3. C.-G. Lee and A. Dodabalapur, *Appl. Phys. Lett.* 96, 243501 (**2010**).
4. S. Jeong, Y. Jeong, and J. Moon, *J. Phys. Chem. C* 112, 11083 (**2008**).
5. F. S. Kim, X. Guo, M. D. Watson, and S. A. Jenekhe, *Adv. Mater.* 22, 478 (**2010**).
6. L. Y. Liang, H. T. Cao, X. B. Chen, Z. M. Liu, F. Zhuge, H. Luo, J. Li, Y. C. Lu, and W. Lu, *Appl. Phys. Lett.* 100, 263502 (**2012**).
7. H. Luo, L. Y. Liang, Q. Liu, and H. T. Cao, *ECS Journal of Solid State Science and Technology* 3, Q3091 (**2014**).
8. E. Fortunato, P. Barquinha, and R. Martins, *Adv. Mater.* 24, 2945 (**2012**).
9. R. Martins, A. Nathan, R. Barros, L. Pereira, P. Barquinha, N. Correia, R. Costa, A. Ahnood, I. Ferreira, and E. Fortunato, *Adv. Mater.* 23, 4491 (**2011**).
10. K. Nomura, T. Kamiya, and H. Hosono, *Adv. Mater.* 23, 3431 (**2011**).
11. Y. Ogo, H. Hiramatsu, K. Nomura, H. Yanagi, T. Kamiya, M. Hirano, and H. Hosono, *Appl. Phys. Lett.* 93, 032113 (**2008**).
12. L. Y. Liang, Z. M. Liu, H. T. Cao, Z. Yu, Y. Y. Shi, A. H. Chen, H. Z. Zhang, Y. Q. Fang, and X. L. Sun, *J. Electrochem. Soc.* 157, H598 (**2010**).
13. P.-C. Hsu, W.-C. Chen, Y.-T. Tsai, Y.-C. Kung, C.-H. Chang, C.-J. Hsu, C.-C. Wu, and H.-H. Hsieh, *Jpn. J. Appl. Phys.* 52, 05DC07 (**2013**).
14. P.-C. Hsu, W.-C. Chen, Y.-T. Tsai, Y.-C. Kung, C.-H. Chang, C.-C. Wu, and H.-H. Hsieh, *Thin Solid Films* 555, 57 (**2014**).
15. J. Um, B. M. Roh, S. Kim, and S. E. Kim, *Mater. Sci. Semiconductor Process* 16, 1679 (**2013**).
16. Y. Kim, J. Um, S. Kim, and S. E. Kim, *ECS Solid State Letters* 1, P29 (**2012**).
17. I.-T. Cho, M. H. U, S.-H. Song, J.-H. Lee, and H.-I. Kwon, *Semicond. Sci. Technol.* 29, 045001 (**2014**).
18. D. C. Paine, B. Yaglioglu, Z. Beiley, and S. Lee, *Thin Solid Films* 516, 5894 (**2008**).
19. K. M. Yu, J. T. Yuh, S. H. K. Park, M. K. Ryu, E. J. Yun, and B. S. Bae, *Jpn. J. Appl. Phys.* 52, 10MA12 (**2013**).
20. L. Schulz, E. J. Yun, and A. Dodabalapur, *Appl. Phys. A* 115, 1103 (**2014**).
21. M. Debucquoy, S. Verlaak, S. Steudel, K. Myny, J. Genoe, and P. Heremans, *Appl. Phys. Lett.* 91, 103508 (**2007**).
22. J. K. Choi, J. M. Song, K. M. Yu, B. S. Bae, and E. J. Yun, *J. Korean Phys. Soc.* 63, 2281 (**2013**).
23. H. Yabuta, N. Kaji, R. Hayashi, H. Kumomi, K. Nomura, T. Kamiya, M. Hirano, and H. Hosono, *Appl. Phys. Lett.* 97, 072111 (**2010**).
24. L. Liang and H. Cao, *ECS Transactions* 50, 289 (**2012**).
25. T. Kamiya and H. Hosono, *NPG Asia Mater.* 2, 15 (**2010**).